Scilight

Nano-electrochemistry & Nano-photochemistry
https://www.sciltp.com/journals/nenp

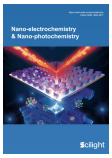

Review

Tailoring Heterojunction Interfaces for Enhanced Photoelectrochemical Biosensing

Chen Zeng, Mingwang Liu * and Aiguo Shen *

School of Biomedical Engineering and Health, Wuhan Textile University, Wuhan 430200, China
* Correspondence: mwliu@wtu.edu.cn (M.L.); agshen@wtu.edu.cn (A.S.)

How To Cite: Zeng, C.; Liu, M.; Shen, A. Tailoring Heterojunction Interfaces for Enhanced Photoelectrochemical Biosensing. *Nano-electrochemistry & Nano-photochemistry* **2026**, *2*(1), 5. https://doi.org/10.53941/nenp.2026.100005

Received: 17 January 2026
Revised: 12 February 2026
Accepted: 25 February 2026
Published: 3 March 2026

Abstract: Photoelectrochemical (PEC) biosensors based on heterojunctions are widely used in bioanalysis for their rapid response and high sensitivity. However, their performance is often limited by inherent interfacial issues, such as poor contact and bandgap mismatch, which constrain the optimization of photoelectric properties and ultimate sensitivity. To address these challenges, recent research has focused on engineering both solid-solid and solid-liquid interfaces. Strategies like enhancing interfacial contact, constructing electron bridges, and promoting surface reactions have proven effective in facilitating carrier separation, migration, and utilization. This review classifies heterojunctions and systematically analyzes how interface design governs carrier behavior and amplifies sensing signals. It further details their applications in biomolecular detection and concludes with future perspectives, highlighting the pivotal role of advanced heterojunction design in propelling PEC sensing technology forward.

Keywords: heterojunctions; interface engineering; signal amplification; photoelectrochemistry; biosensing

1. Introduction

Photoelectrochemical (PEC) sensors represent a novel analytical tool centered on photoactive materials, enabling the identification and detection of target substances by monitoring the photoelectric signals generated when these materials are exposed to light. These sensors offer significant advantages, including ease of miniaturization, low cost, and high sensitivity [1–3]. A key feature of their mechanism is the complete spatial or functional separation between the optical excitation and the electrical readout. Compared to traditional electrochemical or optical methods, this inherent "background noise suppression" effect typically results in higher detection sensitivity [4,5]. The performance of PEC sensors fundamentally depends on the photoreactive materials employed [6]. However, single photoreactive materials often face the issue of limited photoelectric conversion efficiency due to the rapid recombination of photo-generated electron-hole pairs. The construction of heterojunctions is considered one of the key strategies to overcome this bottleneck [7–11]. Formed by the interface contact between two or more semiconductors, heterojunctions typically exhibit strong light absorption capabilities, efficient carrier separation, and rapid interfacial electron transport properties. Due to these advantages, heterojunction engineering has become a core strategy for enhancing the response signals of PEC sensors, demonstrating broad prospects in analytical detection (Figure 1) [6].

Despite their promise, conventional heterojunctions face key practical limitations. A primary issue is the weak interfacial contact caused by intermolecular repulsion between phases, which, coupled with mismatched band structures, creates inefficient and disordered carrier transport paths that favor recombination [12,13]. Furthermore, the interface is prone to defects, dangling bonds, and lattice strain, which act as charge scattering and recombination centers, severely hindering carrier migration [14,15]. These material-level challenges are compounded by the practical requirement to detect target analytes (e.g., biomarkers) at ultralow concentrations in

real samples. Therefore, enhancing PEC sensor sensitivity and signal output through rational heterojunction design remains a critical hurdle in the field [5,16,17].

Recent advances in heterojunction optimization have focused on tailoring both solid-solid and solid-liquid interfaces to enhance charge dynamics and catalytic efficiency. For solid-solid interfaces, strategies primarily aim at steering charge migration pathways and improving interfacial contact. The band alignment configuration plays a crucial role, with S-scheme heterojunctions showing particular promise in directing charge flow and suppressing recombination [18–22]. In addition, optimizing the interfacial contact area and distance or constructing chemical bond-based electron bridges represents an efficient and widely applicable strategy for enhancing interfacial contact [23–35]. Optimizing the solid–liquid interface is essential to accelerate surface reaction kinetics, thereby promoting rapid consumption of photogenerated carriers and preventing their accumulation, which causes recombination or photocorrosion. Introducing functional cocatalysts, such as oxygen reduction reaction (ORR)-active single-atom catalysts (SACs) with atomically dispersed sites and high efficiency, has proven effective [36–38]. For example, Fe-SACs on a photocathode significantly enhance ORR kinetics, facilitate carrier extraction, suppress recombination, and improve photoelectric response [39–41].

In this review, we begin by classifying heterojunctions according to their band alignment configurations. Subsequently, we systematically elaborate on interface engineering strategies aimed at enhancing carrier migration and utilization efficiency, with a focus on both solid-solid and solid-liquid interfaces. Subsequently, the application of heterojunction-based PEC sensors in biomolecular detection is examined, highlighting their pivotal role in enhancing detection sensitivity through representative case studies. Finally, current challenges and prospective research directions in this field are discussed, with the aim of guiding the design of higher-performance heterojunctions and promoting their advanced biosensing applications.

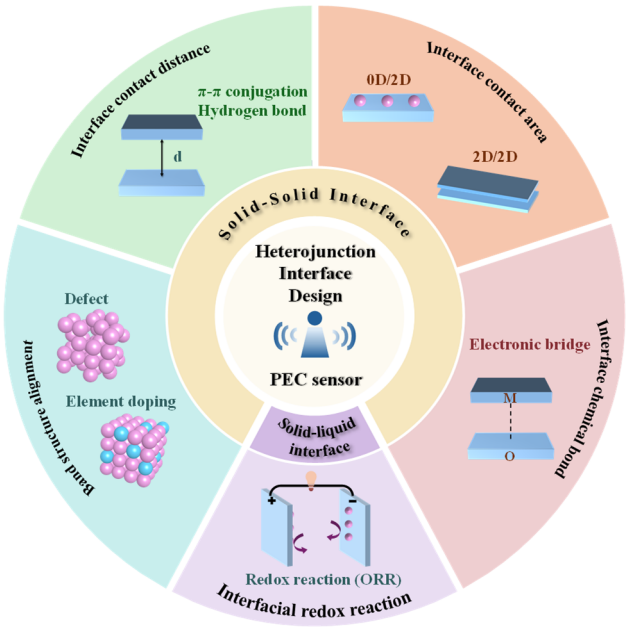

Figure 1. Schematic illustration of heterojunction interface engineering for PEC Sensing.

2. Classification of Heterojunctions

Heterojunctions are categorized into two main types: Schottky junctions formed between metals and semiconductors, and heterojunctions formed between different semiconductors. The fundamental mechanism of Schottky junctions originates from the Schottky barrier, which arises due to the difference in work functions between the metal and semiconductor. This barrier regulates unidirectional charge flow and induces the formation of a built-in electric field (BIEF), thereby facilitating rapid interlayer charge transport [42–44] In the field of PEC sensing, commonly used metals include noble metals with high work functions (such as Au, Pt, and Pd) [45].

Semiconductor heterojunctions have undergone extensive development over time. Since Japanese researchers first employed TiO_2 as a photocatalyst in 1972, photoelectrode materials have evolved from single semiconductors to diverse heterojunction structures [46]. In 2006, Tada et al. proposed the all-solid-state Z-scheme heterojunction, further advancing the field and laying the foundation for the currently widely studied S-scheme heterojunction. Within semiconductor heterojunctions, based on the arrangement of the conduction band (CB) and valence band (VB) energy levels of the two semiconductors, they can be classified into three types: crossed-type, staggered-type,

and broken-belt-type (Figure 2A–C) [10,24]. Among these, the staggered-type has become the most commonly studied due to its ability to achieve efficient carrier separation [10].

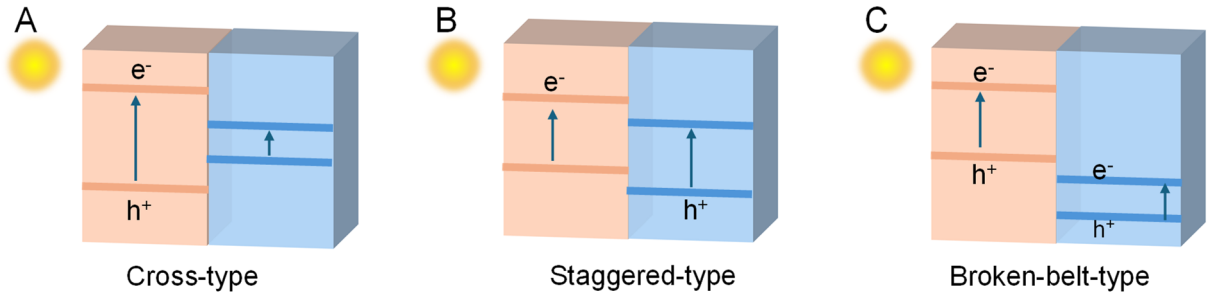

Figure 2. Classification of heterojunctions based on bandgap alignment: (**A**) Cross-type, (**B**) Staggered-type, (**C**) Broken-belt-type.

Based on carrier transport pathways, staggered heterojunctions are primarily classified into conventional Type-II and Step-scheme (S-scheme, evolved from Z-scheme) configurations. In traditional Type-II heterojunctions (Figure 3A), although charge separation is enhanced, the CB electrons retain weak reduction capability, while the VB holes exhibit weak oxidation ability. As a result, the overall photoelectric performance is compromised, limiting broader practical applications [47,48]. To address this, Yu's group elucidated the carrier transport mechanism in S-scheme heterojunctions (Figure 3B) [10,49]. An S-scheme heterojunction typically consists of an oxidation semiconductor (OP) and a reduction semiconductor (RP) with appropriately staggered band alignments. In this configuration, strongly reducing electrons accumulate in the CB of the RP, while strongly oxidizing holes remain in the VB of the OP [10,23,24,32]. This design not only promotes efficient spatial separation of charge carriers but also preserves high redox potentials, thereby significantly enhancing surface reactivity. Consequently, employing S-scheme heterojunctions as electrode materials in the construction of PEC biosensors can substantially improve device performance, offering a promising strategy for achieving highly sensitive detection of bioanalytes.

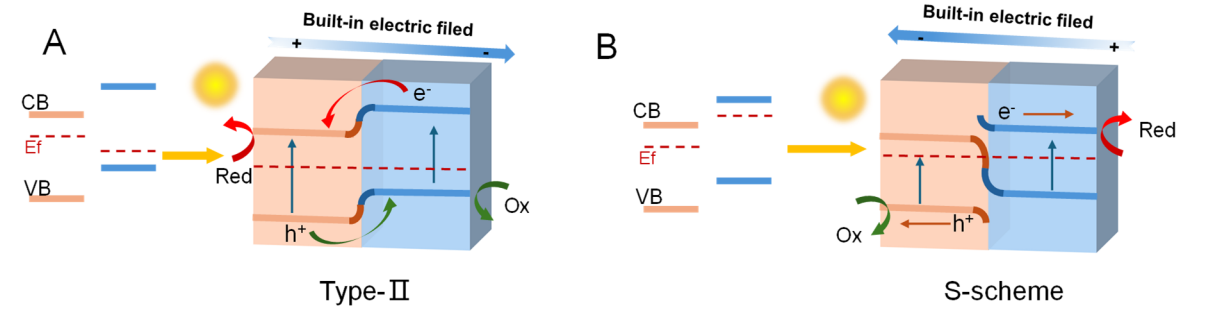

Figure 3. Classification of heterojunctions based on carrier migration paths: (**A**) Type II heterojunction, (**B**) S-scheme heterojunction.

To determine the type of heterojunction formed, three characterization methods are commonly employed: *in situ* X-ray photoelectron spectroscopy (XPS), electron paramagnetic resonance (EPR), and Kelvin probe force microscopy (KPFM). *In situ* XPS monitors the shift of characteristic peaks under illumination compared to dark conditions, reflecting changes in interfacial charge density and thereby enabling inference of charge transfer pathways. EPR directly detects photogenerated reactive species such as $\bullet O_2^-$ or •OH and identifies whether conduction band electrons or valence band holes are involved in the reaction, offering insight into charge separation mechanisms. KPFM utilizes the surface potential measurement capability to evaluate charge transport processes by detecting variations in semiconductor surface potential. Taking an S-scheme heterojunction as an example: under illumination, photogenerated electrons migrate from the oxidized semiconductor to the reduced semiconductor, resulting in an increase in the surface potential of the oxidized component. This potential change, as measured by KPFM, directly corroborates the charge transfer pathway characteristic of the S-scheme heterojunction [49].

3. Interface Design of Heterojunctions

The key to enhancing the performance of PEC sensors lies in improving the separation and utilization of photogenerated carriers. Effective design of both solid-solid and solid-liquid interfaces in heterojunctions can efficiently achieve this goal.

3.1. Solid-Solid Interface

The optimization of solid-solid interfaces in heterojunctions primarily involves two approaches: modulation of the band structure and modification of the contact configuration.

Band structure modulation represents a core strategy for directly influencing the interfacial charge migration behavior in heterojunctions [50]. Current studies demonstrate that the band alignment of heterojunctions can be finely tuned through methods such as defect engineering and elemental doping [51,52]. Typically, chemical processes, including co-precipitation, ion exchange, or thermal decomposition, are employed to decompose or react dopant precursors under controlled conditions. The introduced dopant ions or atoms either substitute for host atoms within the crystal lattice (e.g., Co sites in CoP or metal sites in In_2S_3/CdS) or occupy interstitial positions. This enables precise modulation of the electronic structure, including the d-band center position and BIEF intensity. Consequently, carrier transport pathways in heterojunctions can be rationally optimized toward more efficient Z-scheme or S-scheme configurations. For example, Liu et al. incorporated Zn atoms into CeO_2 via coprecipitation (Figure 4A). By continuously tuning the Fermi level (E_f) of CeO_2 through Zn content variation, they successfully transformed the heterojunction mechanism from type-II (CeO_2/g-C_3N_4) to a highly efficient S-scheme (Figure 4B), resulting in a substantially enhanced photoresponse (Figure 4C) [53]. Similarly, V-atom doping was introduced into In_2S_3 to lower its electronic barrier; when forming a heterojunction with CdS, this approach simultaneously improved interfacial contact and strengthened the BIEF (Figure 4D), thereby significantly enhancing the photoresponse (Figure 4E) [54]. In studies on B-doped g-C_3N_4/CuS and Zn-doped $BiBO_x$/CdS heterojunctions, the Tu's group further demonstrated that elemental doping effectively lowers the E_f of the host semiconductor and enhances the BIEF, leading to improved photogenerated carrier separation and superior photocatalytic degradation of ciprofloxacin [52].

Defect engineering in heterojunctions involves creating vacancies or coordination-deficient sites to disrupt the crystal lattice, which introduces defect energy levels within the bandgap. These defects serve as charge-trapping centers, prolonging carrier lifetime and promoting separation, while simultaneously modifying the band structure to enable more efficient interfacial charge transfer. Moreover, such defect sites often function as active catalytic centers [55–57]. This strategy not only broadens light absorption but also provides effective sites for charge capture and separation, thereby significantly enhancing surface reactivity. For example, the Lin's group established a Z-scheme charge-transfer pathway in a ZrO_2-Pt/Zr-MOF heterojunction through tunable linker defects, achieving a hydrogen production rate of 2923 $\mu mol \cdot g^{-1} \cdot h^{-1}$ [55]. Similarly, Guo et al. utilized oxygen vacancies as electron traps in a ZnCdS/Ov-$NiCo_2O_4$ Schottky heterojunction, where the synergy between the vacancies and the Schottky barrier tripled the hydrogen evolution activity [57]. Furthermore, sulfur vacancies were introduced into an FJU-200/CdS 0D/1D heterojunction (Figure 4F), creating a dual-defect system comprising oxygen vacancies and interfacial S–O bonds that established an efficient Z-scheme pathway (Figure 4G). This modification substantially improved the photoelectric response (Figure 4H) [58].

Heterojunction performance can be improved by optimizing the contact distance and contact area between semiconductors, along with constructing effective interfacial chemical bonds.

Contact distance can be effectively reduced by constructing ultrathin nanosheets or employing *in-situ* growth methods. Among these, van der Waals heterojunctions based on two-dimensional (2D) materials offer a distinctive advantage: they rely on interlayer van der Waals forces rather than traditional band alignment, enabling precise tuning of photoelectric properties through stacking orientation and interlayer coupling [13]. For instance, Liu et al. fabricated a 2D/2D CuTCPP(Cu)/CuTCPP(Fe) (Figure 5A) S-scheme heterojunction via π–π conjugation electrostatic self-assembly (Figure 5B). This design effectively suppresses charge recombination, leading to significantly enhanced photoelectric performance (Figure 5C) [31]. Similarly, Li's group prepared p-COF/p-SiNW S-scheme heterojunctions through *in-situ* solvothermal growth (Figure 5D). The *in-situ* deposition shortened carrier migration distances (Figure 5E), and the interfacial π–π conjugated structure facilitated charge transport. The synergy of these two factors substantially improved the photoresponse (Figure 5F) [59]. The Niu's team achieved intimate contact and favorable band alignment in a 2D in-plane S-scheme HOF/COF heterojunction based on π-conjugated biphenyl units, utilizing hydrogen bonding and π–π stacking interactions [60]. These studies largely leverage the structural features of MOFs, COFs, and HOFs to shorten carrier migration paths through non-covalent interactions such as π–π conjugation and hydrogen bonding. In another example, Wang's group

deposited a conjugated polycarbazole framework (CPF-TCzB) onto the surface of an Sb_2S_3 photoanode, forming a type-II heterojunction with a dense and seamless interface (Figure 5G). This configuration significantly shortened the carrier migration distance, resulting in enhanced photoelectric signals (Figure 5H) [61]. Collectively, these works demonstrate that by judiciously selecting porous framework materials or 2D ultrathin architectures and assembling heterojunctions through appropriate methods, interfacial contact can be optimized to effectively shorten charge migration distances.

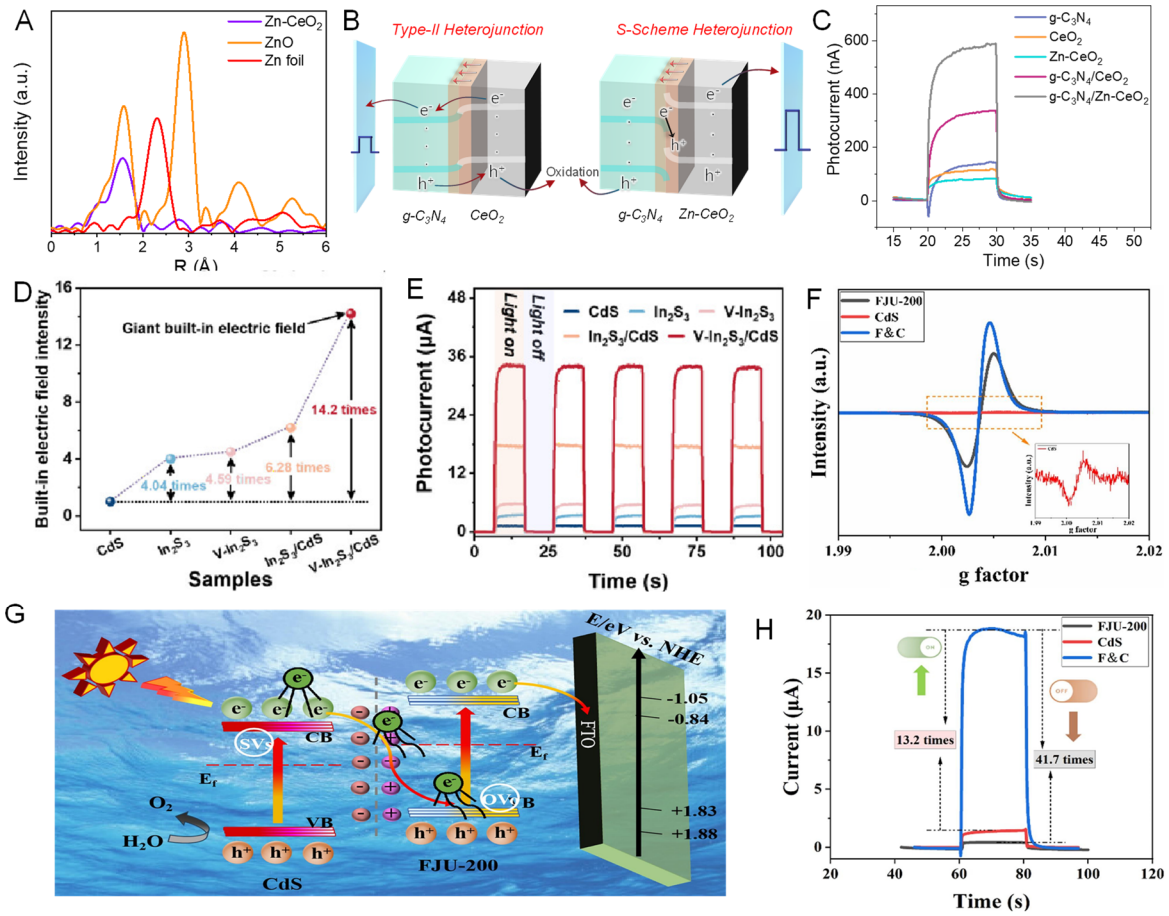

Figure 4. Modulating the band structure of heterojunctions through elemental doping and defect engineering. (**A**) Extended X-ray absorption fine structure spectra. (**B**) Zn doping induces a Type-II to S-scheme heterojunction transition. (**C**) Photocurrent response. Reprinted with permission from [53]. Copyright, 2023, Springer Nature. (**D**) BIEF intensity. (**E**) Photocurrent response of CdS, In_2S_3, V-In_2S_3, In_2S_3/CdS and V-In_2S_3/CdS. Reprinted with permission from [54]. Copyright, 2025, American Chemical Society. (**F**) Electron Spin Resonance spectra of FJU-200, CdS quantum dots, and F&C. (**G**) A 0D/1D heterojunction of FJU-200/CdS featuring dual defects formed by SVs and OVs. (**H**) The photocurrent intensity of FJU-200, CdS quantum dots, and F&C. Reprinted with permission from [58]. Copyright, 2025, Elsevier.

Increasing the contact area of heterojunctions can be effectively achieved by constructing low-dimensional heterojunctions, such as 0D/2D or 2D/2D configurations [31,59,62]. Controlled bottom-up synthesis techniques are commonly employed. These techniques include layer-by-layer assembly, *in-situ* growth, templating, and intercalation. They enable precise design and stabilization of the geometric structure and electronic coupling strength of heterojunction interfaces. Consequently, it avoids random and disordered mixing of the components. Materials such as COFs, MOFs, and HOFs possess high specific surface area and tunable pore structures. These properties make them ideal platforms for such constructions [59]. For example, a 2D/2D biphasic porphyrin-based MOF heterojunction was reported [31], while an S-scheme heterojunction of p-COFs/p-SiNWs was demonstrated, in which photogenerated carriers directionally migrate along the framework [59]. A 2D heterojunction was constructed by *in-situ* growth of porphyrin-based graphdiyne (PDY) on g-C_3N_4 nanosheets, enhancing the sensing signal by 2.54-fold [63]. Additionally, a 2D/2D S-scheme heterojunction based on Py-HOF/Py-COF was developed. Through size matching and interface optimization, its photocatalytic performance reached 9.24 times that of the pure COF [25].

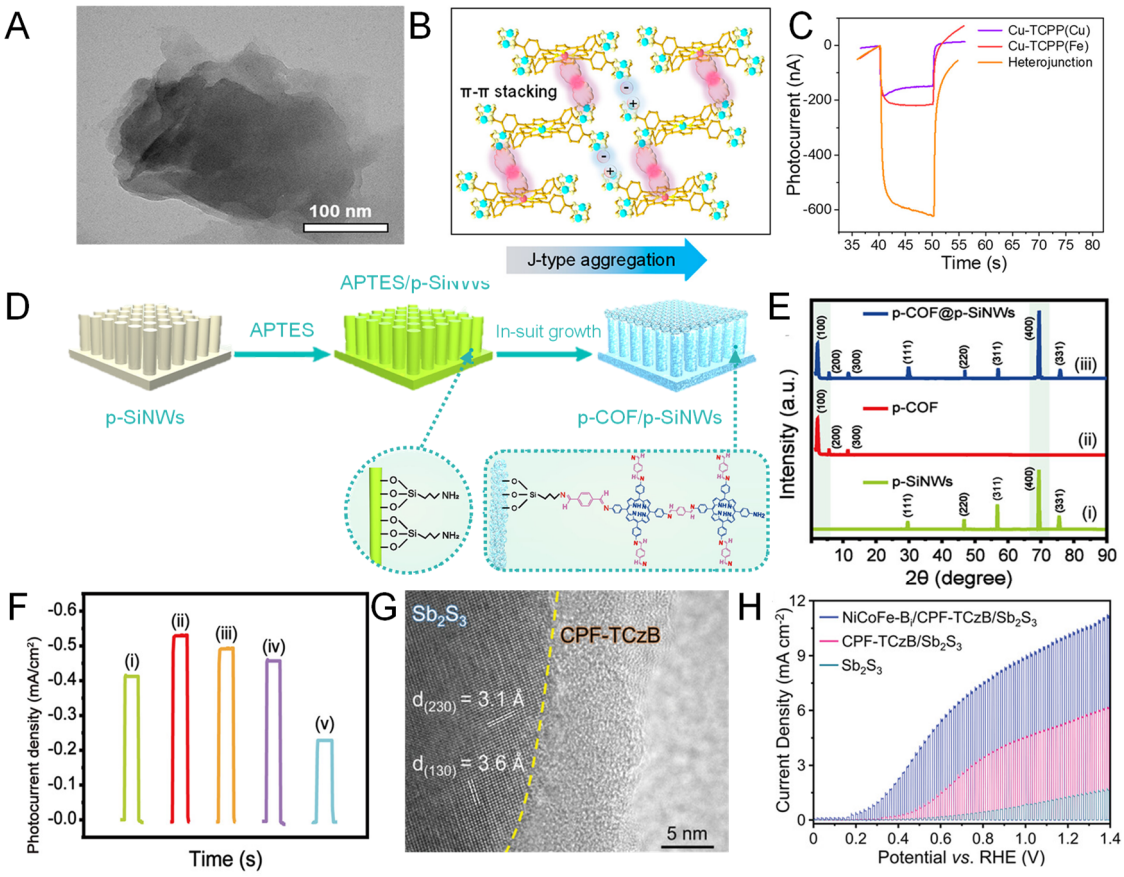

Figure 5. Regulating the contact configuration between semiconductors. Shortening carrier contact distance and increasing contact area: (**A**) Transmission electron microscopy (TEM) image of CuTCPP(Cu)/CuTCPP(Fe) heterojunction. (**B**) Schematic illustration of forming a J-type aggregated heterojunction. (**C**) Photocurrent response. Reprinted with permission from [31]. Copyright, 2023, American Chemical Society. (**D**) In-suit synthesized S-scheme p-COFs/p-SiNWs heterojunction. (**E**) X-ray Diffraction (XRD) patterns. (**F**) Photocurrent responses including (i) p-SiNWs, (ii) p-COF@p-SiNWs, (iii) Anti-cTnI/p-COF@p-SiNWs, (iv) BSA/anti-cTnI/p-COF@p-SiNWs, and (v) cTnI/BSA/anti-cTnI/p-COF@p-SiNWs. Reprinted with permission from [59]. Copyright, 2023, American Chemical Society. (**G**) High-Resolution TEM (HR-TEM) image showing the interface between Sb_2S_3 and CPF-TCzB. (**H**) Current density (J)-potential (V) plots of the Sb_2S_3, CPF-TCzB/Sb_2S_3, and NiCoFe-Bi/CPF-TCzB/Sb_2S_3 photoanodes under simulated one Sun AM 1.5 G chopped illumination. Reprinted with permission from [61]. Copyright, 2022, John Wiley and Sons.

Furthermore, constructing interfacial chemical bonds as "bridges" represents an effective strategy to reduce interfacial barriers and enable atomically directed charge migration [64]. Three principal approaches are used to build such interfacial bonds: first, introducing transition metal atoms (e.g., Co, Ni) at the interface, which leverage their strong coordination with atoms such as O, N, or S to form bridging sites; second, employing precision synthesis to directly link surface atoms of two materials via covalent bonding; and third, utilizing frameworks like MOFs or HOFs as molecular bridges, where anchoring groups at both ends connect the two materials to create directional charge-transfer pathways. For example, Ding et al. integrated Co single atoms into a ZIS/MIL Z-scheme heterojunction, constructing an N–Co–O structure as an atomic-scale charge-transfer bridge. Charge-density difference maps confirmed the effectiveness of this design: in the ZIS/Co/MIL system, electron-depleted (cyan) and electron-enriched (yellow) regions coexisted around the N–Co–O site, indicating an efficient charge-transfer pathway (Figure 6A,B), which significantly enhanced photogenerated carrier separation and PEC performance (Figure 6C) [64]. Similarly, Liu et al. fabricated a Pt–CeO_2/CuTCPP(Fe) p-n heterojunction via atomic-level Pt doping. The doping induced lattice distortion and increased oxygen vacancies, shifting the interfacial bonding from indirect Fe coordination with adsorbed oxygen (Fe-O_A) to direct coordination with lattice oxygen (Fe-O_L) (Figure 6D). This change substantially reduced the energy barrier and distance for charge transfer, leading to a marked improvement in photoresponse (Figure 6E) [65]. He et al. constructed an S-scheme heterojunction (TNZCS) using Ni-doped $Zn_{0.2}Cd_{0.8}S$ quantum dots as the reduction component with TiO_2 microspheres, forming atomic-level Ni–O bonds at the interface. Femtosecond transient absorption spectroscopy

showed that the characteristic decay time constant τ_1 decreased from 66.3 ps to 38.8 ps (Figure 6F,G), directly demonstrating the acceleration of interfacial charge transfer via Ni–O pathways. By synergistically modulating active sites and the BIEF, this heterojunction achieved a significant enhancement in photoelectric response (Figure 6H) [66].

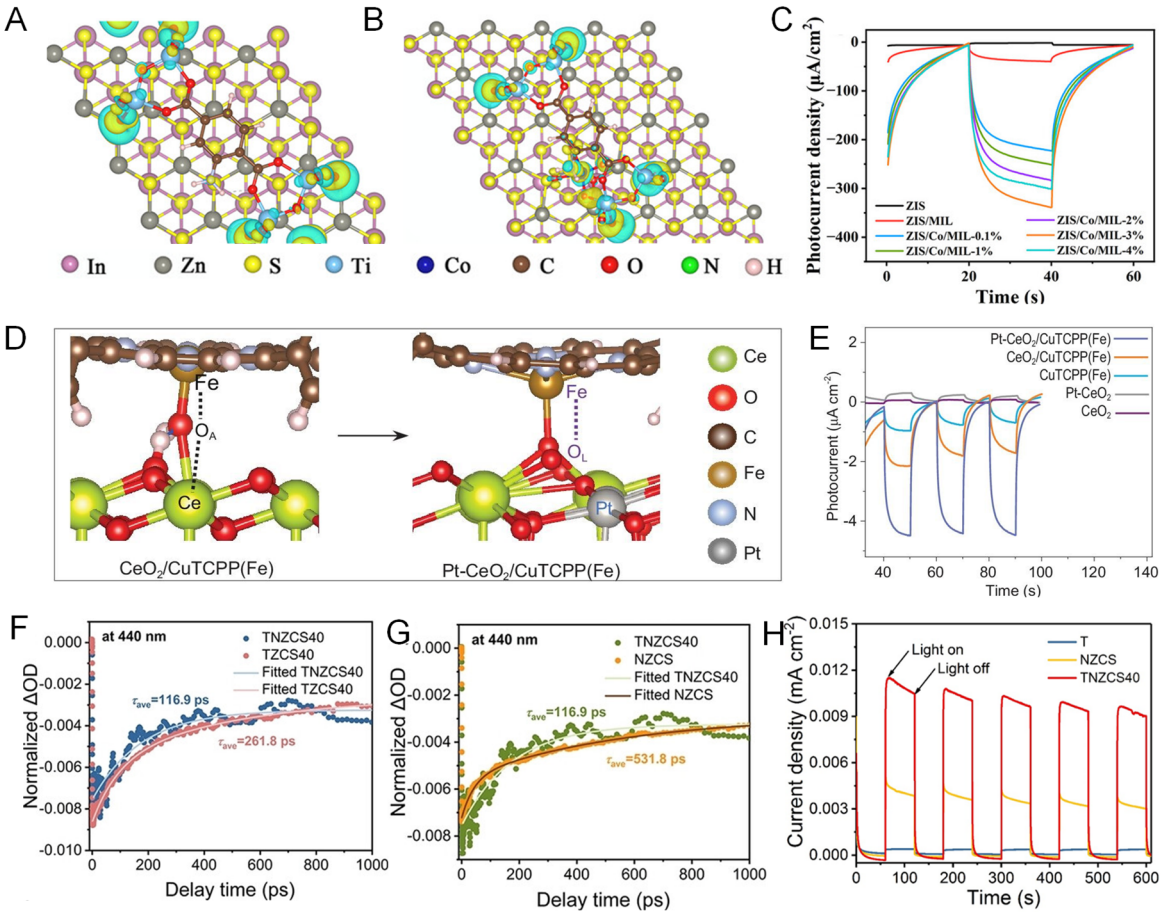

Figure 6. Regulating contact modes between semiconductors. Constructing chemical bonds: The top view of charge density difference of (**A**) ZIS/MIL and (**B**) ZIS/Co/MIL. (**C**) Photocurrent response of ZIS, ZIS/MIL, and ZIS/Co/MIL. Reprinted with permission from [64]. Copyright, 2025, John Wiley and Sons. (**D**) Schematic illustration of the interfacial Fe-O bond in different *p-n* junctions. (**E**) Photocurrent response of photoactive materials. Reprinted with permission from [65]. Copyright, 2024, Oxford University Press. (**F**,**G**) Corresponding fitted transient absorption kinetics of GSB peaks at 440 nm in ZCS, NZCS, and TNZCS40 within 1000 ps. (**H**) Transient photocurrent density of as-prepared samples measured under intermittent Xe lamp illumination. Reprinted with permission from [66]. Copyright, 2023, John Wiley and Sons.

Additionally, interfacial engineering can optimize charge migration through the design of a "charge extraction layer". This intermediate functional layer, typically composed of materials with tailored energy-level structures such as Pt nanoclusters, is introduced between the semiconductor and the co-catalyst. Its primary role is to regulate the electron transport pathway, enabling efficient directional charge extraction. This approach not only suppresses interfacial recombination but also promotes the transfer of photogenerated electrons to catalytically active sites [67–69]. For instance, the Zhu team developed an innovative interfacial engineering strategy by constructing a composite co-catalyst (Pt NC/Fe–N–C) on the surface of p-type CuO semiconductors [67]. The co-catalyst consists of Pt nanoclusters (Pt NCs) supported on nitrogen-doped carbon with Fe–N–C sites. In this architecture, Pt NCs function as an efficient charge extraction layer, forming atomic-scale Pt–Fe bonding channels between CuO and Fe–N–C (Figure 7A). This structure significantly accelerates the interfacial extraction of photogenerated carriers. The design simultaneously optimizes charge transfer efficiency at the solid–solid interface and oxygen reduction kinetics at the solid–liquid interface, leading to a substantial enhancement in photoelectric performance (Figure 7B). This strategy requires careful band alignment between the extraction layer and the semiconductor: in n-type systems, the hole extraction layer must exhibit a low-energy band and low E_f to establish effective hole migration pathways (Figure 7C); in p-type systems, the extraction layer requires a higher E_f to facilitate electron transfer (Figure 7D) [67].

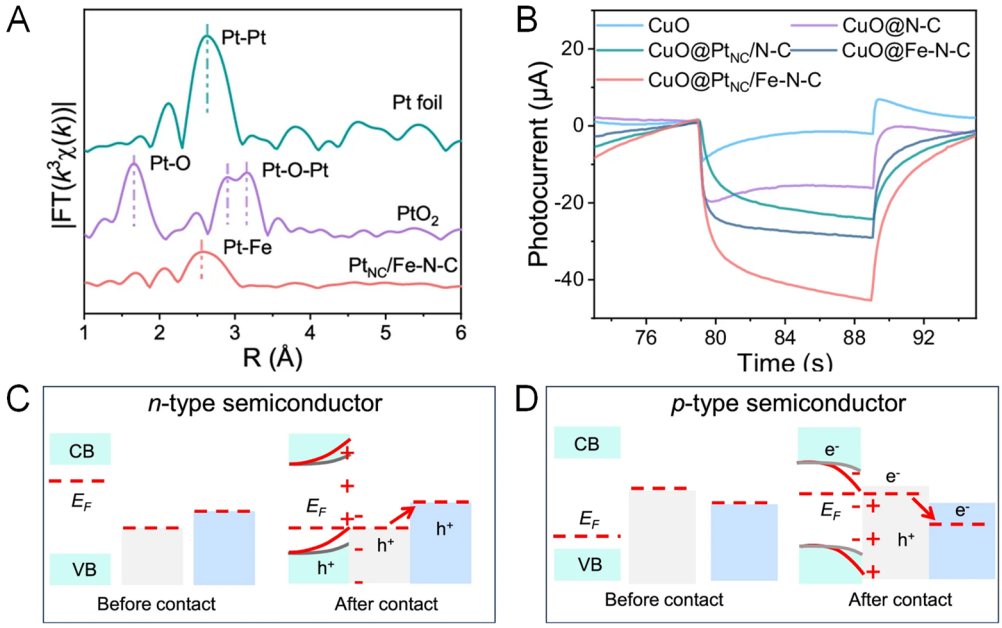

Figure 7. Optimizing charge migration pathways by constructing charge extraction layers. (**A**) Nonphase-corrected Fourier-transformed Extended X-Ray Absorption Fine Structure spectra at Pt L_3-edge. (**B**) Photocurrent responses for CuO, CuO@N-C, CuO@Pt_{NC}/N-C, CuO@Fe-N-C, and CuO@Pt_{NC}/Fe-N-C. (**C**) A charge extraction layer constructed for an n-type semiconductor. (**D**) A charge extraction layer formed with a p-type semiconductor. Reprinted with permission from [67]. Copyright, 2025, Springer Nature.

In recent years, research focus has shifted from conventional type-II heterojunctions toward more advantageous Z-scheme or S-scheme heterojunction systems. The core mechanism for constructing efficient heterojunctions lies in establishing a strong BIEF that spatially separates photogenerated electron–hole pairs, thereby reducing carrier recombination and enhancing PEC activity. Additional merits include improved light-absorption capacity and the preservation of high redox potentials [14]. Liu et al. constructed a dual S-scheme heterojunction Bi_2O_3–BiOBr–AgI. Combined with light-controlled selective deposition, this design achieves precise spatial separation between oxidation sites (Bi_2O_3) and reduction sites (AgI). This architecture successfully mimics the electron-transport chain in natural photosynthetic systems (Figure 8A), leading to a significant enhancement in performance (Figure 8B) [70]. Similarly, a $Cu_2S/CdIn_2S_4$ Z-scheme heterojunction (CS/CIS) with a hierarchical hollow cubic structure was fabricated via *in-situ* growth and annealing transformation (Figure 8C). The heterojunction exhibited greatly enhanced photocatalytic activity: its photocurrent density increased approximately sixfold compared to hollow Cu_2S cubes and nearly tenfold relative to snowflake-like Cu_2S, outperforming most reported Cu_2S- and $CdIn_2S_4$-based materials (Figure 8D) [71]. Yang's group integrated an S-scheme heterojunction with a Schottky barrier by loading gold nanoparticles onto a covalent S-scheme heterojunction. The covalent S-scheme heterojunction (PHI-PDI) primarily optimizes intralayer charge separation and migration, while the Schottky barrier (Au/PHI-PDI) enhances interlayer charge transport and suppresses carrier recombination (Figure 8E). The optimal catalyst, 3% Au/PHI-PDI, achieved a CO production rate of 122.65 $\mu mol \cdot g^{-1} \cdot h^{-1}$, which is 2.77 times that of PHI-PDI and 9.24 times that of PHI (Figure 8F) [43]. Collectively, these studies demonstrate that rational design of the heterojunction band structure can exploit the BIEF and band-bending effects to effectively suppress photogenerated carrier recombination and improve separation efficiency. Moreover, the strategic integration of S-scheme heterojunctions with Schottky junctions to construct multi-heterojunction systems offers a promising route to achieve synergistic performance gains beyond the capabilities of individual structures [72,73].

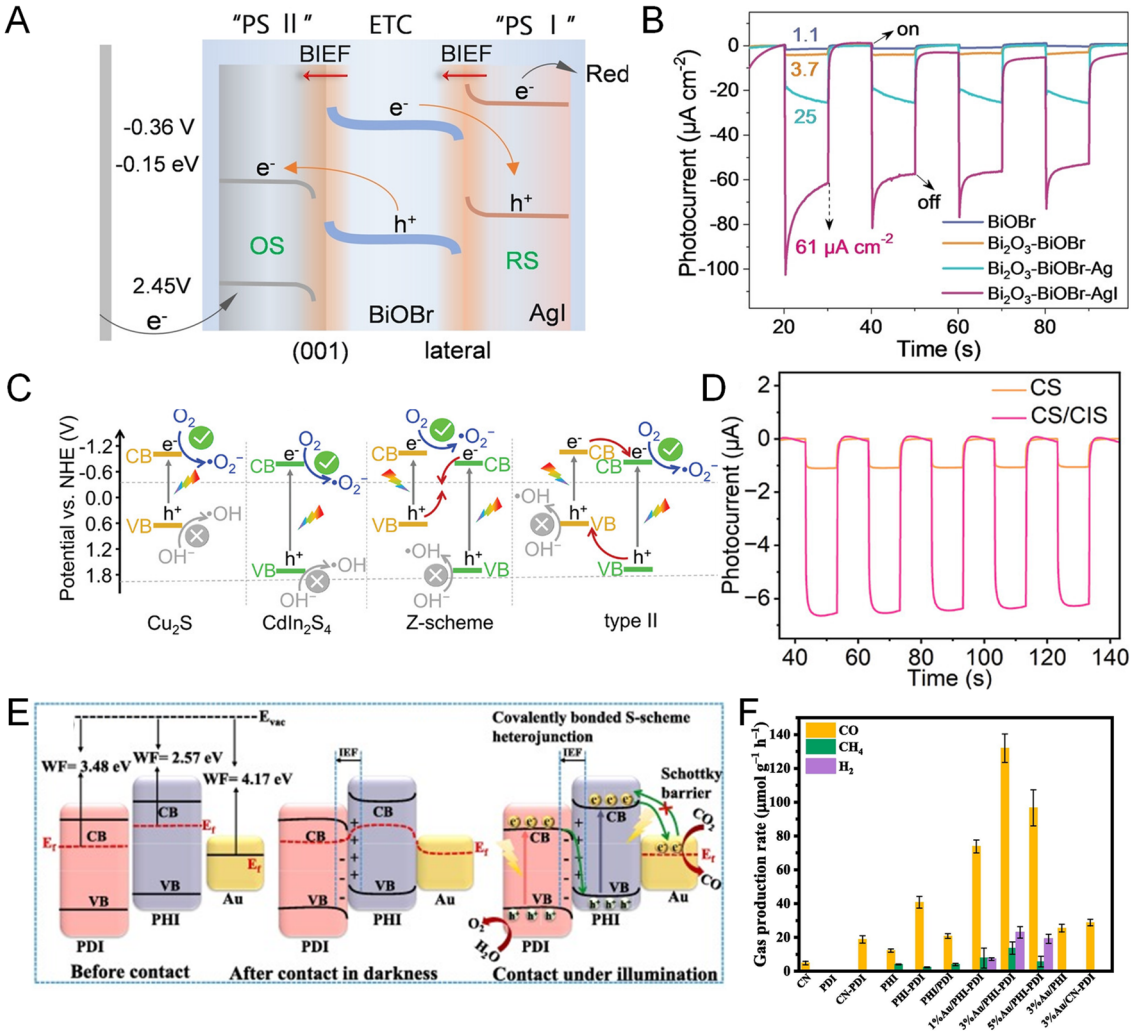

Figure 8. (**A**) Charge transfer path schematic diagram of Bi_2O_3-BiOBr-AgI. (**B**) Photocurrent response of BiOBr, Bi_2O_3-BiOBr, Bi_2O_3-BiOBr-Ag, and Bi_2O_3-BiOBr-AgI. Reprinted with permission from [70]. Copyright, 2024, John Wiley and Sons. (**C**) Schematic illustration of charge transfer in Cu_2S cubes, $CdIn_2S_4$, Z-scheme heterojunction, and type II heterojunction. (**D**) Transient photocurrent responses of hollow Cu_2S cubes modified ITO and CS/CIS/ITO in PBS. Reprinted with permission from [71]. Copyright, 2024, John Wiley and Sons. (**E**) The schematic illustration of Au/PHI-PDI before and after contact, and under illumination. (**F**) CO production rates over different photocatalysts. Reprinted with permission from [43]. Copyright, 2025, Elsevier.

3.1. Solid-Liquid Interface

In PEC sensing, optimizing the solid–liquid interface between the electrode and the electrolyte is as critical as tuning the solid–solid interface. Introducing an efficient external ORR represents a key strategy to accelerate interfacial carrier extraction and consumption, enhance reaction kinetics, and ultimately improve signal output. The underlying mechanism involves the continuous consumption of electrons by the ORR at the interface, thereby accelerating the utilization of effective charge carriers.

For instance, Qin et al. significantly improved the carrier dynamics of p-type CuO by modifying it with Ni single atoms supported on carbon (NiSA@C) (Figure 9A). Under illumination in O_2-saturated electrolyte, the photocurrent increased markedly, indicating that the ORR effectively consumes photogenerated electrons, suppresses recombination, and thus enhances the photocurrent. In contrast, under N_2-saturated conditions, the photocurrent remained low even under illumination (Figure 9B), confirming the essential role of ORR in photocurrent enhancement [74]. They also fabricated a high-performance photocathode by integrating Fe-SACs with a $Cu_2O/Ti_3C_2T_x$ composite (Figure 9C). The Fe-SACs effectively accelerated the interfacial ORR rate, promoting the consumption of photogenerated electrons. This reduced charge accumulation and significantly boosted the photocurrent. In O_2-saturated electrolyte, the photocurrent response was substantially higher than in N_2-saturated medium, directly confirming the pivotal role of the ORR process (Figure 9D) [41]. Similarly, Tan et al. modified a dual-function Fe-SACs onto a $CdS/CuInS_2$ dual-photoelectrode system, greatly improving its PEC conversion

efficiency and enabling a novel dual-photoelectrode PEC fuel cell [75]. Chen et al. incorporated Pt NC/Fe–N–C onto p-type CuO. Benefiting from charge transfer between Pt nanoclusters and Fe single atoms, the ORR activity at the Fe sites was significantly enhanced. Electrochemical measurements showed that Pt NC/Fe–N–C exhibited a more positive half-wave potential ($E_{1/2}$) than Fe–N–C alone (Figure 9E), indicating superior ORR kinetics. This effectively increased the interfacial oxygen reduction rate (Figure 9F), accelerated the consumption and transfer of photogenerated electrons, suppressed electron–hole recombination, and substantially enhanced the photocurrent signal [67]. These studies demonstrate that SACs, as highly efficient ORR catalysts, can significantly enhance PEC signal responses through the above-described mechanisms.

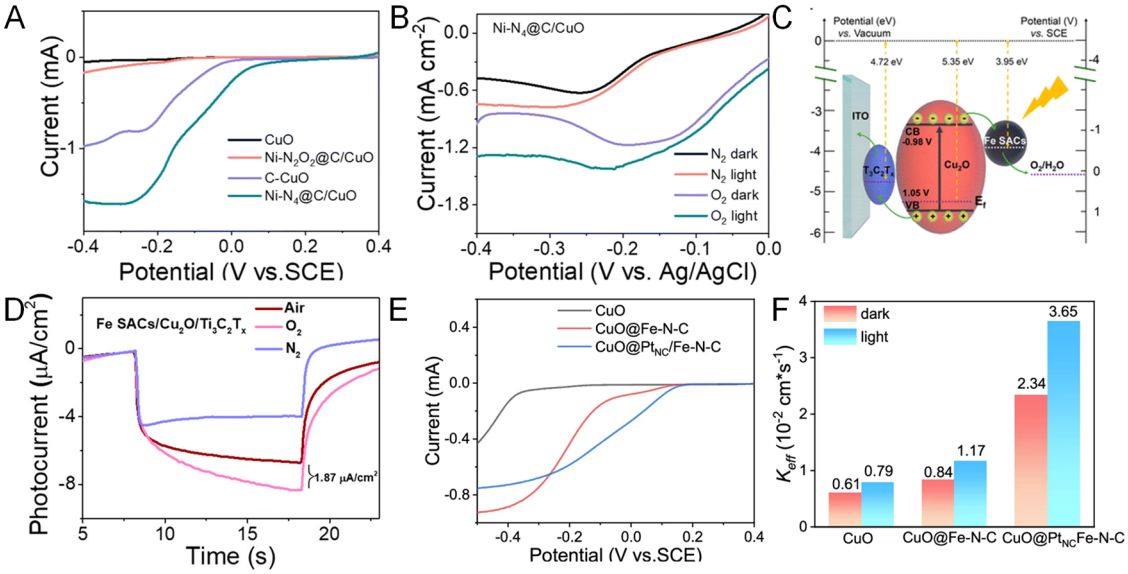

Figure 9. Micro-scale regulation of heterojunction solid-liquid interfaces. (**A**) The ORR polarization curves of CuO, Ni-N_2O_2@C/CuO, C/CuO, and Ni-N_4@C/CuO in 0.1 M PBS (pH = 7.4). (**B**) LSV (with and without light) of Ni-N_4@C/CuO in the O_2 and N_2 saturated-buffer electrolyte, respectively. Theoretical calculation of O_2 adsorption and the side view of the charge density difference on. Reprinted with permission from [74]. Copyright, 2023, Royal Society of Chemistry. (**C**) Schematic energy band diagram. (**D**) Photocurrent responses of Fe-SACs/Cu_2O/$Ti_3C_2T_x$ in the air, O_2, and N_2 saturated-buffer electrolyte, respectively. Reprinted with permission from [41]. Copyright, 2022, American Chemical Society. (**E**) The ORR polarization curves of CuO, CuO@Fe-N-C, and CuO@Pt_{NC}/Fe-N-C in 0.1 M PBS (pH = 7.4). (**F**) Rate constant (Keff) of different samples under light and dark conditions. Reprinted with permission from [67]. Copyright, 2025, Springer Nature.

Furthermore, the design of the heterojunction solid-liquid interface has significantly enhanced the long-term stability and anti-interference capability of the sensor. These performance improvements are attributed to the continuous and efficient electron consumption mechanism of the ORR at the interface. On one hand, the ORR accelerates the extraction and utilization of photogenerated electrons, thereby reducing the recombination of photogenerated carriers and effectively suppressing photocorrosion and activity degradation of the electrode materials. On the other hand, as the dominant reaction pathway at the interface, the high selectivity of the ORR minimizes competition from other substances in complex samples for the same reaction sites and prevents disruption of the electron transfer chain. This ensures signal specificity when the sensor is exposed to multiple coexisting species [67].

4. Application of Heterojunctions in PEC Biosensing

Precise detection of biomolecules is fundamental to advancing medical and health technologies, relying on highly sensitive and specific real-time monitoring of dynamic changes in biomarkers such as proteins and nucleic acids. This necessitates the development of next-generation sensing technologies with exceptional sensitivity, stability, and resistance to contamination. Against this backdrop, heterojunction interface engineering has emerged as a core strategy for achieving these goals. By rationally controlling the interface structure of heterojunctions, charge separation and transport efficiency can be significantly enhanced, thereby amplifying PEC responses and improving detection sensitivity. Simultaneously, optimized interfaces improve material photostability and

suppress non-specific adsorption, ultimately enhancing sensor robustness against interference and reliability in real-world samples [76–78].

4.1. Biomacromolecules

Biomacromolecules primarily include proteins (e.g., antibodies, enzymes, hormones, and structural proteins), peptides, nucleic acids, polysaccharides, and related compounds. PEC sensing enables highly sensitive detection of these biomacromolecules. For example, targeting the TET1 protein, Zheng's group developed a PEC biosensor based on a Bi_2O_3/Bi_2S_3/MXene type-II heterojunction. By exploiting the intrinsic catalytic activity of the target protein, the sensor achieved efficient detection with a linear response of I(nA) = −97.3 logc(μg/mL) − 230 and a detection limit of 0.014 μg/mL (Figure 10A) [79]. A sandwich-type immunosensor employing a $ZnIn_2S_4$/g-C_3N_4 heterostructure was constructed for the detection of carcinoembryonic antigen, utilizing $BiVO_4$ labels to introduce a steric hindrance effect [80]. For cardiac injury markers, Li et al. designed an S-scheme p-COF@p-SiNW heterojunction sensor to detect cardiac troponin I (cTnI) (Figure 10B). The sensor exhibited a wide linear range from 5 pg/mL to 10 ng/mL and a low detection limit of 1.36 pg/mL in clinical serum, offering a promising tool for early and precise diagnosis of myocardial infarction (Figure 10C) [59]. Additionally, they constructed a 1D/2D Cu-TCPP/$BiVO_4$ heterojunction that recognizes miRNA-133a through immobilized probes [81]. Furthermore, Zhu's team utilized the peroxidase-like activity of a Pt–CeO_2/CuTCPP(Fe) p-n junction to develop a PEC immunoassay for prostate-specific antigen (PSA) (Figure 10D). This design cleverly couples the intrinsic enzyme-mimetic activity of the heterojunction with pH modulation mediated by exogenous glucose oxidase (GOx), establishing a dual-signal-amplification mechanism. The assay achieves ultrasensitive PSA detection at the pg/mL level while maintaining high selectivity and excellent analytical performance (Figure 10E) [65].

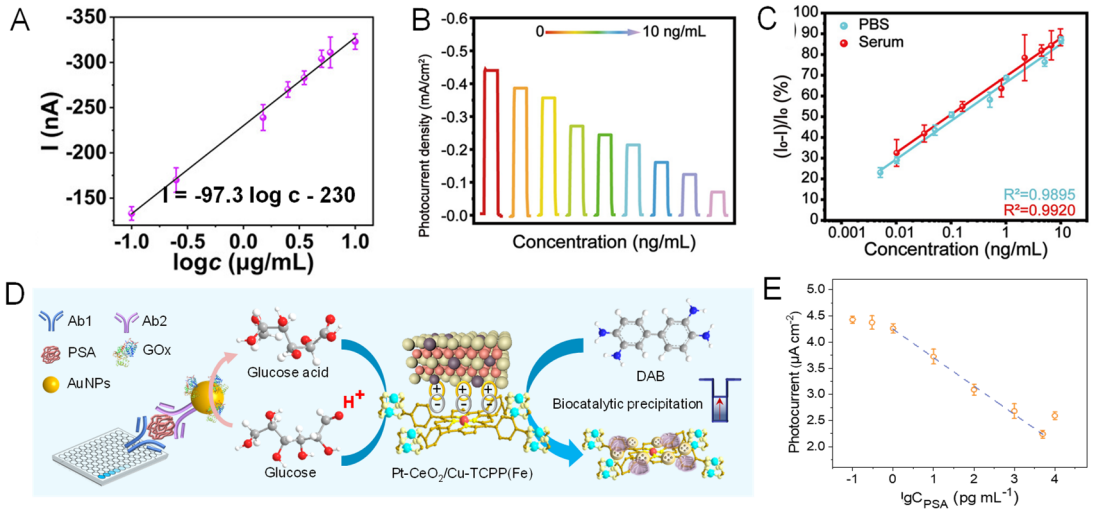

Figure 10. (**A**) Linear relationship between the photocurrent and the logarithm value of TET1 protein concentration. Direct linear relationship between photocurrent and concentration of TET1 protein against the value. Reprinted with permission from [79]. Copyright, 2022, American Chemical Society. (**B**) Photocurrent responses for the detection of cTnI at different concentrations. (**C**) Calibration plots between $(I_0 - I)/I_0$ and the logarithm of cTnI concentration, where the error bars are standard deviations for n = 3. Reprinted with permission from [59]. Copyright, 2023, American Chemical Society. (**D**) Mechanism diagram of the PEC immunosensor for PSA detection. (**E**) Logarithmic calibration curve of the PEC immunosensor within the range of 1–5000 pg mL^{-1} (LOD: 0.71 pg/mL). Reprinted with permission from [65]. Copyright, 2024, Oxford University Press.

Enzyme-based biosensors have emerged as another significant direction in PEC bioanalysis, serving as powerful tools for qualitative and quantitative analysis of multiple targets in disease diagnosis and biomedical research [82]. For instance, a Zn-atom doping strategy was employed to transform the CeO_2/g-C_3N_4 heterojunction from a Type-II to an S-scheme configuration, and a corresponding PEC biosensor was constructed for acetylcholinesterase (AChE) detection (Figure 11A). This sensor detection system exhibits a linear detection range of 5–1600 mU·mL^{-1} for AChE, with a limit of detection of 3.2 mU·mL^{-1} (Figure 11B). It demonstrates excellent linear response and high sensitivity across a broad concentration range, further enabling smartphone-based portable semi-quantitative detection [53]. They further developed a Bi_2O_3-BiOBr-AgI dual S-scheme heterojunction system for high-performance analysis of the AChE (Figure 11D). The photocurrent exhibits a good

linear relationship with the logarithm of enzyme activity (Figure 11C). Further studies demonstrate that the constructed Bi_2O_3-BiOBr-AgI dual S-scheme heterojunction enables highly sensitive detection of organophosphorus pesticides, achieving a detection limit as low as 0.15 ng/mL. In comparison, the Bi_2O_3-BiOBr-Ag heterojunction sensor exhibits a detection limit of 1.8 ng/mL, representing an improvement in sensitivity by more than an order of magnitude. This comparison underscores the critical role of interfacial engineering strategies in enhancing sensing performance [70]. An *in-situ* sensitized PEC biosensor was constructed based on silane-functionalized carbon nitride (SP-C_3N_4) electrodes (Figure 11E), which enabled sensitive detection of α-glucosidase (α-Glu) activity with good linearity over the range of 0.5 to 80 mU/mL (Figure 11F) [83]. The studies described above have all achieved notable sensitivity.

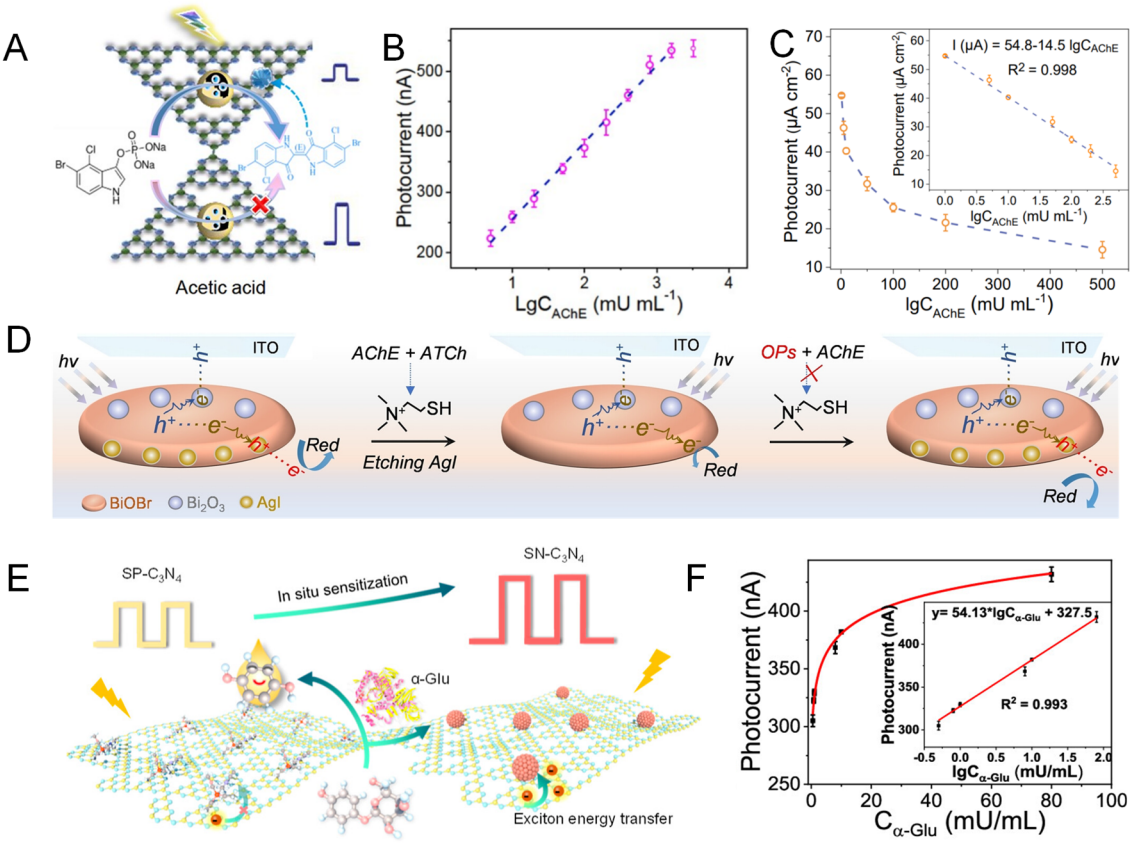

Figure 11. Enzyme activity detection examples: (**A**) AChE PEC biosensor based on Zn-CeO_2/g-C_3N_4 S-scheme heterojunction (LOD: 3.2 mU/mL). (**B**) AChE detection based on a biomimetic artificial photosynthesis system (LOD: 0.15 ng/mL). Reprinted with permission from [53]. Copyright, 2023, Springer Nature. (**C**) Calibration curve of the Bi_2O_3-BiOBr-AgI-based PEC sensor within the range of 1–500 mU mL^{-1} for the AChE activity. Error bars are based on the standard deviation of the mean (n = 3). (**D**) Mechanism diagram of the PEC sensor for AChE and OPs detection. Reprinted with permission from [70]. Copyright, 2024, John Wiley and Sons. (**E**) Glucose oxidase detection via PEC biosensing using an *in-situ* sensitization strategy (LOD: 0.1 mU/mL). (**F**) The fitted linear relationship between photocurrent responses and α-Glu concentration in the concentration range of 0.5–80 mU/mL. Reprinted with permission from [83]. Copyright, 2023, American Chemical Society.

4.2. Biological Small Molecules

Biological small molecules primarily include metabolic intermediates and end-products (e.g., glucose, lactate, uric acid), signaling molecules (such as dopamine, cortisol), reactive species (e.g., H_2O_2), as well as certain vitamins and pharmaceutical compounds.

For metabolic intermediates like glucose, one study developed a microwave-assisted green-synthesis method to prepare 2D graphene oxide/manganese vanadium oxide (MnV_2O_6/GO) nanosheet composites, enabling highly selective PEC detection of glucose with a limit of detection as low as 0.13 μM (Figure 12A) [84]. Another work reported a π-π-conjugation-enhanced and interface-matched 2D bimetallic porphyrin MOF-on-MOF S-scheme heterojunction (CuTCPP(Cu)/CuTCPP(Fe)) for PEC uric acid sensing (Figure 12B), which exhibited a wide linear range (0.2–400 μM) and a low detection limit of 0.12 μM (Figure 12C) [31]. In terms of signaling-molecule detection, a label-free, highly sensitive dopamine sensor was developed using $BiVO_4$/C_3N_4 heterojunction-based

photoactive gate materials. The platform showed a broad linear response from 10^{-7} to 10^{-4} M with a detection limit of 10^{-7} M, achieving approximately three orders of magnitude signal enhancement through a dual-amplification mechanism [85]. For reactive species such as H_2O_2, CdSe/ZnS quantum dots combined with TiO_2 nanocomposites were employed. By coating the quantum dots with ultrathin TiO_2 layers via atomic layer deposition to form QD–TiO_2 heterojunctions, carrier recombination within the quantum dots was effectively suppressed, resulting in a 90-fold increase in photocurrent and a detection limit as low as 10 μM [86]. More advanced explorations focus on integrated diagnostic-therapeutic systems. For instance, one study designed Fe_1–Zn_1–TiO_2 dual-single-atom photoelectrodes for real-time *in vivo* monitoring of the anticancer drug methotrexate (MTX), successfully constructing an implantable closed-loop "monitoring–feedback–treatment" platform (Figure 12D). The sensor demonstrated high sensitivity (detection limit 0.684 μM) and a wide linear range (1–100 μM), fully covering the clinical therapeutic window of MTX at both low-dose (6–16 μM) and high-dose (25–60 μM) regimens, indicating excellent clinical applicability (Figure 12E) [87]. Additionally, a label-free PEC aptasensor based on a Cu_2MoS_4@$Ti_3C_2T_x$ MXene heterojunction was developed for highly sensitive and selective detection of tetracycline in milk [88]. In summary, through deliberate heterojunction engineering, PEC sensors have achieved highly sensitive detection of diverse biomolecules, highlighting their considerable potential for analyzing complex biological systems.

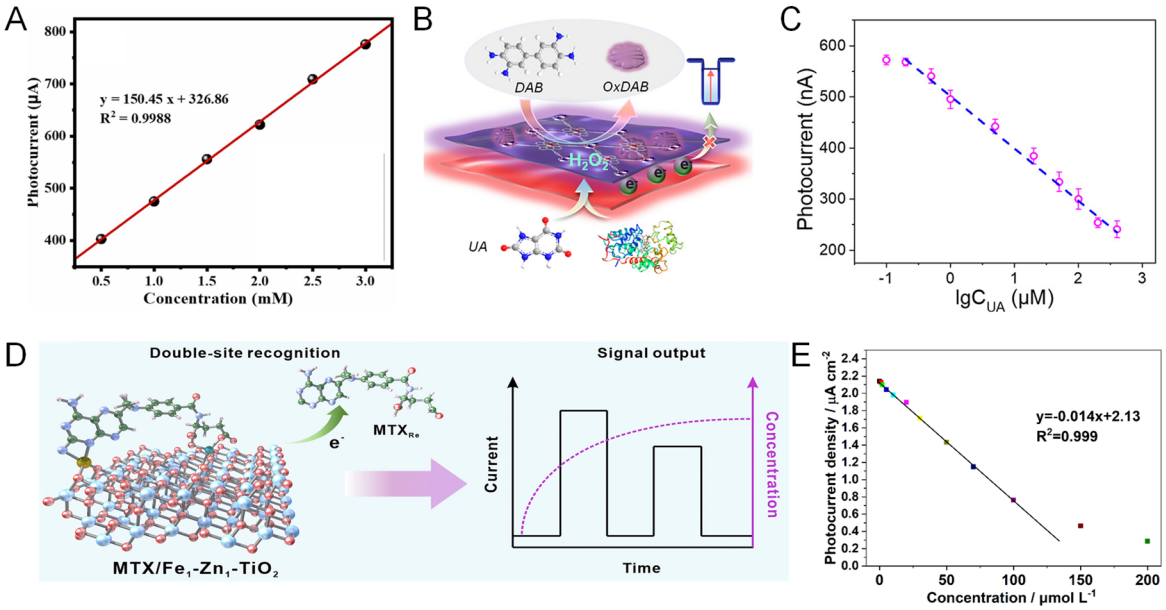

Figure 12. Detection of Biomolecular Small Molecules. (**A**) Linear fitting of different scan rates of glucose during PEC measurement. Reprinted with permission from [84]. Copyright, 2025, Elsevier. (**B**) Uric acid PEC sensor based on MOF-on-MOF S-scheme heterojunction (CuTCPP(Cu)/CuTCPP(Fe)). (**C**) The logarithmic calibration curve of the PEC sensor is within the range of 0.1–400 mU mL^{-1}. Reprinted with permission from [31]. Copyright, 2023, American Chemical Society. (**D**) Dual single-atom photoelectrode (Fe_1-Zn_1-TiO_2) for *in vivo* real-time monitoring and closed-loop drug delivery systems. (**E**) PEC linear calibration curves of MTX in the range of 0–100 μM. Reprinted with permission from [87]. Copyright, 2025, Springer Nature.

Table 1. Correlation between heterojunction types, interface design and sensing functions.

Heterojunction Types	Interface Strategies	Enhancing Sensing Functions	Ref.
Type-II	Electron bridge	Sensitivity	[79]
S-scheme	π–π conjugation Elemental doping	Sensitivity and stability	[31,53,59]
p-n junction	Atomic-level chemical bonds	Sensitivity	[65]
Dual S-scheme	Mimicking natural photosynthesis	Sensitivity and selectivity	[70]
Schottky heterojunction	0D/2D	Sensitivity	[88]

5. Summary and Outlook

Given the superior performance of heterojunctions in PEC sensing, various heterojunction types have significantly contributed to enhancing sensor sensitivity. This paper reviews recent research advances in heterojunction-based PEC biosensing, focusing on interfacial design methods and signal enhancement strategies. The high performance of heterojunctions depends not only on their intrinsic types (e.g., Type II, S-scheme, Schottky junctions) but also critically relies on precise "engineered" control of their interfaces. A core future challenge lies in achieving precise atomic/nanoscale interface construction to overcome issues such as interface state recombination centers introduced by lattice mismatch and dangling bonds. This requires deep integration of *in-situ* characterization techniques and theoretical calculations to dynamically analyze charge transfer processes, thereby guiding the design of "defect-controlled" heterojunctions. By synergistically optimizing solid-solid and solid-liquid interfaces, it is possible to fundamentally enhance carrier separation and transport efficiency while accelerating interfacial reaction kinetics. However, transitioning from ideal conditions to practical applications presents significant challenges for heterojunction materials in complex biological environments, including photocorrosion, biofouling, and long-term stability. Developing bio-inspired interface coatings with anti-fouling and self-cleaning capabilities, while elucidating their photochemical stability mechanisms in real samples, is crucial for advancing practical applications. Furthermore, achieving miniaturization and intelligent operation of PEC biosensors requires efficient integration of heterojunction photoelectrodes with microfluidics, wireless transmission, and energy management modules. However, current research predominantly focuses on the material level, leaving a significant gap between materials science and device applications. Future efforts should prioritize developing flexible, stretchable heterojunction photoelectrodes, exploring low-power and self-powered designs, and constructing multi-signal fusion sensing architectures to enhance detection reliability and practicality. For *in vivo* and dynamic monitoring applications, heterojunction systems must overcome limitations in spectral response range and biocompatibility. Specifically, developing near-infrared-responsive, biodegradable heterojunction materials and establishing *in vivo* performance and safety evaluation standards are critical steps toward this goal.

In summary, heterojunction interface design serves as the bridge connecting high-performance materials with practical biosensing applications. By continuously deepening our understanding of interfacial physicochemical processes and integrating cutting-edge technologies from materials science, photoelectric, biomedicine, and micro/nano fabrication, we can expect to pioneer smarter, more integrated, and practical next-generation PEC biosensors. These innovations will play increasingly critical roles in precision medicine, point-of-care diagnostics, and real-time monitoring. Looking ahead, PEC biosensors will deeply integrate micro-nano fluidics, flexible electronics, and artificial intelligence algorithms, evolving into highly integrated, user-friendly smart home devices. This will ultimately enable one-touch precision testing with "sample-in, result-out" functionality. Such devices will serve as real-time intelligent front-end systems for personal health, seamlessly connecting with home and healthcare networks via the Internet of Things. This will drive a fundamental shift in disease monitoring-transitioning from traditional hospital-based diagnostics to a routine, proactive prevention paradigm within the home environment.

Funding

The authors gratefully acknowledge the financial support of the National Natural Science Foundation of China (No. 22504106).

Conflicts of Interest

The authors declare no conflict of interest.

Use of AI and AI-Assisted Technologies

No AI tools were utilized for this paper.

References

1. Zhao, W.-W.; Xu, J.-J.; Chen, H.-Y. Photoelectrochemical DNA Biosensors. *Chem. Rev.* **2014**, 114, 7421–7441.
2. Zhao, W.-W.; Xu, J.-J.; Chen, H.-Y. Photoelectrochemical Immunoassays. *Anal. Chem.* **2018**, 90, 615–627.
3. Yan, K.; Ji, W.; Zhu, Y.; et al. Photofuel Cell Coupling with Redox Cycling as a Highly Sensitive and Selective Self-Powered Sensing Platform for the Detection of Tyrosinase Activity. *Chem. Commun.* **2019**, 55, 12040–12043.
4. Li, H.; Li, Y.; Li, J.; et al. Magnetic–Optical Core–Shell Nanostructures for Highly Selective Photoelectrochemical Aptasensing. *Anal. Chem.* **2020**, 92, 4094–4100.

5. Li, Q.; Zhou, Q.; Wu, Y.; et al. Dual S-Scheme Heterojunction via MOF-on-MOF Strategy for Efficient Photoelectrocatalytic Removal of Organic Contaminants: Detoxification and Mechanism. *J. Environ. Sci.* **2025**, 155, 111–126.
6. Liu, X.; Yang, D.; Liu, B.; et al. Progress in Signal Amplification and Microstructure Manufacturing for Photoelectrochemical Sensing. *Annu. Rev. Anal. Chem.* **2025**, 18, 383–405.
7. Nishiyama, H.; Yamada, T.; Nakabayashi, M.; et al. Photocatalytic Solar Hydrogen Production from Water on a 100-m^2 Scale. *Nature* **2021**, 598, 304–307.
8. Zhang, H.; Gao, Y.; Meng, S.; et al. Metal Sulfide S-Scheme Homojunction for Photocatalytic Selective Phenylcarbinol Oxidation. *Adv. Sci.* **2024**, 11, 2400099.
9. Wang, G.; Xu, J.; Chen, H. Progress in the Studies of Photoelectrochemical Sensors. *Sci. China Chem.* **2009**, 52, 1789–1800.
10. Zhang, L.; Zhang, J.; Yu, J.; et al. Charge-Transfer Dynamics in S-Scheme Photocatalyst. *Nat. Rev. Chem.* **2025**, 9, 328–342.
11. Loka, C.; Gelija, D.; Vattikuti, S.V.P.; et al. Silver-Boosted WO_3/$CuWO_4$ Heterojunction Thin Films for Enhanced Photoelectrochemical Water Splitting Efficiency. *ACS Sustain. Chem. Eng.* **2023**, 11, 11978–11990.
12. Wang, Y.; Li, J.; Zhou, Y.; et al. Interfacial Defect Mediated Charge Carrier Trapping and Recombination Dynamics in TiO_2-Based Nanoheterojunctions. *J. Alloys Compd.* **2021**, 872, 159592.
13. Zhang, Q.; Li, M.; Li, L.; et al. Recent Progress in Emerging Two-Dimensional Organic–Inorganic van der Waals Heterojunctions. *Chem. Soc. Rev.* **2024**, 53, 3096–3133.
14. Zhang, S.; Du, P.; Lu, X. Advancements in Semiconductor-Based Interface Engineering Strategies and Characterization Techniques for Carrier Dynamics in Photoelectrochemical Water Splitting. *Sci. China Mater.* **2024**, 67, 1379–1392.
15. Mao, Y.; Wang, P.; Zhan, S. Shedding Light on the Role of Interfacial Chemical Bond in Heterojunction Photocatalysis. *Nano Res.* **2022**, 15, 10158–10170.
16. Wang, H.; Li, C.; Zhang, J.; et al. NIR-Excitable POM-Encapsulated Yb-Bi_2S_3 Decorated Graphene for Wearable Photoelectrochemical Sensing. *Adv. Funct. Mater.* **2024**, 34, 2315917.
17. Jiang, J.; Wu, T.; Wei, M.; et al. Self-Powered Photoelectrochemical Sensing for Sensitive Detection of Chloramphenicol Based on Sulfur-Vacancy Engineered MoS_2 Nanoribbons/Plasmonic Ti_3C_2 MXene with Continual Injection of Photoinduced Electrons. *J. Environ. Chem. Eng.* **2024**, 12, 112067.
18. Zhang, W.; Mohamed, A.R.; Ong, W.-J. Z-Scheme Photocatalytic Systems for Carbon Dioxide Reduction: Where Are We Now? *Angew. Chem. Int. Ed.* **2020**, 59, 22894–22915.
19. Wang, Y.; Tang, J.; Peng, Z.; et al. Fully Solar-Powered Photoelectrochemical Conversion for Simultaneous Energy Storage and Chemical Sensing. *Nano Lett.* **2014**, 14, 3668–3673.
20. Liu, Y.; Liu, J.; Zhang, Q.; et al. CuO/Ag_2S/CuS Nanohybrids-Integrated Photoelectric and Photothermal Effects for Ultrasensitive Detection of Inorganic Pyrophosphatase. *Adv. Funct. Mater.* **2022**, 32, 2106854.
21. Liu, S.; Jia, Y.; Li, Y.; et al. Separation of Biological Events from the Photoanode: Toward the Ferricyanide-Mediated Redox Cyclic Photoelectrochemical System of an Integrated Photoanode and Photocathode. *ACS Sens.* **2020**, 5, 3540–3546.
22. Li, F.; Wang, S.; Yin, H.; et al. Photoelectrochemical Biosensor for DNA Formylation Detection in Genomic DNA of Maize Seedlings Based on Black TiO_2-Enhanced Photoactivity of MoS_2/WS_2 Heterojunction. *ACS Sens.* **2020**, 5, 1092–1101.
23. Fu, J.; Xu, Q.; Low, J.; et al. Ultrathin 2D/2D WO_3/g-C_3N_4 Step-Scheme H_2-Production Photocatalyst. *Appl. Catal. B Environ. Energy* **2019**, 243, 556–565.
24. Dhakshinamoorthy, A.; Li, Z.; Yang, S.; et al. Metal–Organic Framework Heterojunctions for Photocatalysis. *Chem. Soc. Rev.* **2024**, 53, 3002–3035.
25. Gao, R.; Shen, R.; Huang, C.; et al. 2D/2D Hydrogen-Bonded Organic Frameworks/Covalent Organic Frameworks S-Scheme Heterojunctions for Photocatalytic Hydrogen Evolution. *Angew. Chem. Int. Ed.* **2025**, *64*, e202414229.
26. Lu, Y.; Zhuang, Z.; Li, L.; et al. Advancements and Challenges in g-C_3N_4/$ZnIn_2S_4$ Heterojunction Photocatalysts. *J. Mater. Chem. A* **2025**, 13, 4718–4745.
27. Ma, Y.; Cai, D.; Wan, S.; et al. Ladder-Type Heteroheptacenes with Different Heterocycles for Nonfullerene Acceptors. *Angew. Chem. Int. Ed.* **2020**, 59, 21627–21633.
28. Jing, J.; Yang, J.; Li, W.; et al. Construction of Interfacial Electric Field via Dual-Porphyrin Heterostructure Boosting Photocatalytic Hydrogen Evolution. *Adv. Mater.* **2022**, 34, 2106807.
29. Babu, S.S.; Praveen, V.K.; Ajayaghosh, A. Functional π-Gelators and Their Applications. *Chem. Rev.* **2014**, 114, 1973–2129.
30. Xie, W.; Chen, Y.; Hu, D.; et al. Chlorinating the π-Extended Central Core of Nonfullerene Acceptor Enables High-Performance Polymer Solar Cells. *Chem. Eng. J.* **2025**, 523, 168450.
31. Liu, M.; Wen, J.; Xiao, R.; et al. Improving Interface Matching in MOF-on-MOF S-Scheme Heterojunction through π–π Conjugation for Boosting Photoelectric Response. *Nano Lett.* **2023**, 23, 5358–5366.
32. Wang, C.; Zhao, Y.; Cheng, C.; et al. S-Scheme Heterojunction Photocatalysts: Mechanism, Challenges and Opportunities. *Coord. Chem. Rev.* **2024**, 521, 216177.
33. Li, H.; Tong, H.; Zhang, J.; et al. Oxygen Vacancy Induced Atom-Level Interface in Z-Scheme SnO_2/$SnNb_2O_6$ Heterojunctions for Robust Solar-Driven CO_2 Conversion. *ACS Appl. Mater. Interfaces* **2023**, 15, 36179–36189.

34. Li, H.; Shi, J.; Deng, J.; et al. Intermolecular π–π Conjugation Self-Assembly to Stabilize Surface Passivation of Highly Efficient Perovskite Solar Cells. *Adv. Mater.* **2020**, 32, 1907396.
35. Chae, S.Y.; Jun, M.; Yoon, N.; et al. Origin of Enhanced Photoelectrochemical Activity of the N-CdS/p-Type Semiconductor Interface: Homojunction or Heterojunction? *Small* **2025**, 21, 2405048.
36. Kumar, A.; Gil-Sepulcre, M.; Fandré, J.P.; et al. Regulating Local Coordination Sphere of Ir Single Atoms at the Atomic Interface for Efficient Oxygen Evolution Reaction. *J. Am. Chem. Soc.* **2024**, 146, 32953–32964.
37. Jeong, H.; Kwon, O.; Kim, B.-S.; et al. Highly Durable Metal Ensemble Catalysts with Full Dispersion for Automotive Applications beyond Single-Atom Catalysts. *Nat. Catal.* **2020**, *3*, 368–375.
38. Shan, J.; Ye, C.; Jiang, Y.; et al. Metal-Metal Interactions in Correlated Single-Atom Catalysts. *Sci. Adv.* **2022**, *8*, eabo0762.
39. Cai, Q.; Li, H.; Li, Z.; et al. Single-Atom Iron Boosts Interfacial Oxygen Reduction for Self-Powered Photoelectrochemical Biosensing. *Anal. Chem.* **2025**, *97*, 17580–17588.
40. Xu, C.; Guo, C.; Liu, J.; et al. Accelerating the Oxygen Adsorption Kinetics to Regulate the Oxygen Reduction Catalysis via Fe_3C Nanoparticles Coupled with Single Fe-N_4 Sites. *Energy Storage Mater.* **2022**, *51*, 149–158.
41. Qin, Y.; Wen, J.; Wang, X.; et al. Iron Single-Atom Catalysts Boost Photoelectrochemical Detection by Integrating Interfacial Oxygen Reduction and Enzyme-Mimicking Activity. *ACS Nano* **2022**, *16*, 2997–3007.
42. Shen, Z.; Pu, M.; Xie, Y.; et al. Precise Construction of S-Scheme and Dual Schottky Junctions in g-C_3N_5/TiO_2-O_v@Ti_3C_2 Ternary Heterojunction for Efficient Visible-Light Acetaminophen Degradation: Enhanced Oriented Charge Migration. *Chem. Eng. J.* **2025**, *525*, 170199.
43. Yang, R.; Li, Q.; Ma, Z.; et al. Improving Charge Separation in Poly (Heptazine Imide) via Synergy of Covalent S-Scheme Heterojunction and Schottky Junction for Efficient Photocatalytic CO_2 Reduction. *Chem. Eng. J.* **2025**, *506*, 160043.
44. Wang, G.; Sun, Y.; Yang, Z.; et al. Near-Ideal Schottky Junction Photodetectors Based on Semimetal-Semiconductor van der Waals Heterostructures. *Adv. Funct. Mater.* **2024**, *34*, 2316267.
45. Jimenéz-Calvo, P.; Muñoz-Batista, M.J.; Isaacs, M.; et al. A Compact Photoreactor for Automated H_2 Photoproduction: Revisiting the (Pd, Pt, Au)/TiO_2 (P25) Schottky Junctions. *Chem. Eng. J.* **2023**, *459*, 141514.
46. Fox, M.A.; Tien, T.P. Photoelectrochemical Detector for High-Pressure Liquid Chromatography. *Anal. Chem.* **1988**, *60*, 2278–2282.
47. Low, J.; Yu, J.; Jaroniec, M.; et al. Heterojunction Photocatalysts. *Adv. Mater.* **2017**, *29*, 1601694.
48. Tada, H.; Mitsui, T.; Kiyonaga, T.; et al. All-Solid-State Z-Scheme in CdS–Au–TiO_2 Three-Component Nanojunction System. *Nat. Mater.* **2006**, *5*, 782–786.
49. Xu, Q.; Zhang, L.; Cheng, B.; et al. S-Scheme Heterojunction Photocatalyst. *Chem* **2020**, *6*, 1543–1559.
50. Pan, Y.; Sun, K.; Lin, Y.; et al. Electronic Structure and d-Band Center Control Engineering over M-Doped CoP (M = Ni, Mn, Fe) Hollow Polyhedron Frames for Boosting Hydrogen Production. *Nano Energy* **2019**, *56*, 411–419.
51. He, F.; Lu, Y.; Jiang, G.; et al. Unveiling the Dual Charge Modulation of Built-in Electric Field in Metal-Free Photocatalysts for Efficient Photo-Fenton-like Reaction. *Appl. Catal. B Environ. Energy* **2024**, *341*, 123307.
52. Tu, B.; Miao, J.; Che, R.; et al. Regulation of Built-in Electric Field in Heterojunction for Improved Photocatalytic Degradation of Ciprofloxacin: Role of Element Doping. *Sep. Purif. Technol.* **2025**, *352*, 128188.
53. Liu, M.; Wen, J.; Qin, Y.; et al. Metal Atom Doping-Induced S-Scheme Heterojunction Boosts the Photoelectric Response. *Sci. China Chem.* **2023**, *66*, 1228–1236.
54. Qin, J.; Wu, D.; Yu, Z.; et al. Modulating Built-In Electric Field Strength in an In_2S_3/CdS Heterojunction via Vanadium Doping for a Photoelectrochemical Immunoassay. *Anal. Chem.* **2025**, *97*, 23631–23639.
55. Lin, Y.-M.; Cheng, W.-W.; Zhang, L.-C.; et al. Defects Calculation and Accelerated Interfacial Charge Transfer in a Photoactive MOF-Based Heterojunction. *Small* **2025**, *21*, 2411388.
56. Xiong, R.; Sun, Y.; Huang, J.; et al. Defect-Engineered WO_{3-x}@$Zn_3In_2S_{6-x}$ S-Scheme Heterojunction with Atomic Interfacial Bonds for Efficient Photothermal-Assisted Photocatalytic H_2O_2 Production. *Chem. Eng. J.* **2025**, *519*, 164909.
57. Guo, X.; Fan, L.; Liu, J.; et al. Built-in Electric Field and Oxygen Vacancy Defects in ZnCdS/O_v-$NiCo_2O_4$ Schottky Heterojunction to Achieve Efficient Photocatalytic Hydrogen Evolution. *Appl. Catal. B Environ. Energy* **2025**, *378*, 125586.
58. Mao, C.; Ju, C.; Wang, H.; et al. Dual Vacancy Defect-Enhanced FJU-200/CdS Heterojunction for Ultrasensitive Photoelectrochemical Detection of CA19-9: Mechanism and Performance Study. *Chem. Eng. J.* **2025**, *505*, 159934.
59. Li, H.-J.; Huang, Y.; Zhang, S.; et al. S-Scheme Porphyrin Covalent Organic Framework Heterojunction for Boosted Photoelectrochemical Immunoassays in Myocardial Infarction Diagnosis. *ACS Sens.* **2023**, *8*, 2030–2040.
60. Niu, H.; Zhu, G.; Zhang, S.; et al. Enhanced Photocatalytic Hydrogen Production by Built-in Electric Field in Self-Assembled HOF–WO_3 S-Scheme Heterojunctions. *Chem. Eng. J.* **2025**, *525*, 170181.
61. Wang, L.; Lian, W.; Liu, B.; et al. A Transparent, High-Performance, and Stable Sb_2S_3 Photoanode Enabled by Heterojunction Engineering with Conjugated Polycarbazole Frameworks for Unbiased Photoelectrochemical Overall Water Splitting Devices. *Adv. Mater.* **2022**, *34*, 2200723.
62. Zhu, B.; Sun, J.; Zhao, Y.; et al. Construction of 2D S-Scheme Heterojunction Photocatalyst. *Adv. Mater.* **2024**, *36*, 2310600.

63. Niu, Y.; Xie, D.; Wei, S.; et al. g-C_3N_4/Porphyrin-Based Graphdiyne (PDY) 2D/2D Heterojunction for the Ultrasensitive Photoelectrochemical Detection of microRNA-21. *Sci. China Chem.* **2024**, *409*, 135653.
64. Ding, W.; Yu, H.; Yin, J.; et al. Engineering Atomically Precise Cobalt Charge-Transfer Bridges for Cascade Amplification-Enhanced Photoelectrochemical Sensing. *Adv. Funct. Mater.* **2025**, *36*, e18134.
65. Liu, M.; Yang, W.; Xiao, R.; et al. Lattice Atom-Bridged Chemical Bond Interface Facilitates Charge Transfer for Boosted Photoelectric Response. *Natl. Sci. Rev.* **2025**, *12*, nwae465.
66. He, B.; Xiao, P.; Wan, S.; et al. Rapid Charge Transfer Endowed by Interfacial Ni–O Bonding in S-Scheme Heterojunction for Efficient Photocatalytic H_2 and Imine Production. *Angew. Chem. Int. Ed.* **2023**, *62*, e202313172.
67. Chen, Y.; Qin, Y.; Liu, M.; et al. Pt Nanocluster-Fe Single Atom Pairs Dual-Regulate Charge Extraction and Interfacial Reaction for Enhanced Photoelectric Response. *Nat. Commun.* **2025**, *16*, 2960.
68. Zhang, J.; Pan, Y.; Feng, D.; et al. Mechanistic Insight into the Synergy between Platinum Single Atom and Cluster Dual Active Sites Boosting Photocatalytic Hydrogen Evolution. *Adv. Mater.* **2023**, *35*, 2300902.
69. Laskowski, F.A.L.; Oener, S.Z.; Nellist, M.R.; et al. Nanoscale Semiconductor/Catalyst Interfaces in Photoelectrochemistry. *Nat. Mater.* **2020**, *19*, 69–76.
70. Liu, M.; Yang, W.; Xiao, R.; et al. Anisotropic Dual S-Scheme Heterojunctions Mimic Natural Photosynthetic System for Boosting Photoelectric Response. *Angew. Chem. Int. Ed.* **2024**, *63*, e202407481.
71. Zhang, S.; Sun, J.; Ju, H. Z-Scheme Heterojunction of Hierarchical $Cu_2S/CdIn_2S_4$ Hollow Cubes to Boost Photoelectrochemical Performance. *Small* **2024**, *20*, 2405712.
72. Ghosh, R.; Singh, M.; Chang, L.W.; et al. Enhancing the Photoelectrochemical Hydrogen Evolution Reaction through Nanoscrolling of Two-Dimensional Material Heterojunctions. *ACS Nano* **2022**, *16*, 5743–5751.
73. Monsalve, Y.; Cruz-Pacheco, A.F.; Orozco, J. Plasmonic Graphene–Gold Nanostar Heterojunction for Red-Light Photoelectrochemical Immunosensing of C-Reactive Protein. *ACS Sens.* **2025**, *10*, 1493–1504.
74. Qin, Y.; Tan, R.; Wen, J.; et al. Engineering the Microenvironment of Electron Transport Layers with Nickel Single-Atom Sites for Boosting Photoelectrochemical Performance. *Chem. Sci.* **2023**, *14*, 7346–7354.
75. Tan, R.; Qin, Y.; Liu, M.; et al. Bifunctional Single-Atom Iron Cocatalysts Enable an Efficient Photoelectrochemical Fuel Cell for Sensitive Biosensing. *Adv. Funct. Mater.* **2023**, *33*, 2305673.
76. Zhao, J.; Tian, J.; Zhang, X.; et al. Innovative Nanozyme-Based Detection Methods for Biomarkers in Interstitial Fluid. *TrAC Trends Anal. Chem.* **2025**, *189*, 118248.
77. Li, Z.; Guo, M.; Zhong, W. Multiplex Detection of Biomarkers Empowered by Nanomaterials. *Precis. Chem.* **2025**, *3*, 297–318.
78. Hsu, Y.-P.; Li, N.-S.; Pang, H.-H.; et al. Lab-on-the-Needles: A Microneedle Patch-Based Mobile Unit for Highly Sensitive *Ex Vivo* and *In Vivo* Detection of Protein Biomarkers. *ACS Nano* **2025**, *19*, 3249–3264.
79. Zheng, Y.; Cui, X.; Zhou, Y.; et al. MXene Enhanced Photoactivity of Bi_2O_3/Bi_2S_3 Heterojunction with G-Wire Superstructure for Photoelectrochemical Detection of TET1 Protein. *ACS Sens.* **2022**, *7*, 3116–3125.
80. Bo, Y.; Li, L.; Miao, P.; et al. 2D Z-Scheme $ZnIn_2S_4$/g-C_3N_4 Heterojunction Based on Photoelectrochemical Immunosensor with Enhanced Carrier Separation for Sensitive Detection of CEA. *Biosens. Bioelectron.* **2024**, *247*, 115926.
81. Li, H.-J.; Huang, C.; Wang, F.; et al. Photo-Nanozyme-Integrated Photoelectrochemical-Electrochemical Dual-Mode Biosensor: Enabling Amplification-Free Detection of miRNA-133a in Acute Myocardial Infarction. *Anal. Chem.* **2025**, *97*, 6686–6693.
82. Zhao, W.-W.; Xu, J.-J.; Chen, H.-Y. Photoelectrochemical Enzymatic Biosensors. *Biosens. Bioelectron.* **2017**, *92*, 294–304.
83. Qin, Y.; Zhang, J.; Tan, R.; et al. Small-Molecule Probe-Induced *In Situ*-Sensitized Photoelectrochemical Biosensor for Monitoring α-Glucosidase Activity. *ACS Sens.* **2023**, *8*, 3257–3263.
84. Jrar, J.A.; Bilal, M.; Butt, F.K.; et al. A Novel 2D Graphene Oxide/Manganese Vanadium Oxide Nanocomposite-Based PEC Biosensor for Selective Detection of Glucose. *J. Alloys Compd.* **2025**, *1021*, 179595.
85. Cai, T.; Zhang, W.; Charlton, F.; et al. $BiVO_4/C_3N_4$ Heterojunction-Gated Organic Photoelectrochemical Transistor for Sensitive Detection of Neurotransmitter. *Biosens. Bioelectron.* **2025**, *280*, 117444.
86. Zhao, S.; Yue, Z.; Zhu, D.; et al. Quantum Dot/TiO_2 Nanocomposite-Based Photoelectrochemical Sensor for Enhanced H_2O_2 Detection Applied for Cell Monitoring and Visualization. *Small* **2024**, *20*, 2401703.
87. Xu, X.; Xu, D.; Zhou, X.; et al. Implantable Photoelectrochemical-Therapeutic Methotrexate Monitoring System with Dual-Atomic Docking Strategy. *Nat. Commun.* **2025**, *16*, 1747.
88. Xu, Y.; Chen, L.; Guo, X.; et al. Highly Sensitive Label-Free Photoelectrochemical Aptasensor Based on Cu_2MoS_4@$Ti_3C_2T_x$ MXene Heterojunction for Tetracycline Detection in Milk. *Microchim. Acta* **2025**, *192*, 165.